Research Square

Preprints are preliminary reports that have not undergone peer review.
They should not be considered conclusive, used to inform clinical practice,
or referenced by the media as validated information.

The reasons capacity loss in Li-ion battery with anatase - rutile anode under the cycling

Katherine Dmytrivna Pershina

katherinepersh@gmail.com

V I Vernadsky Institute of General and Inorganic Chemistry National Academy of Sciences of Ukraine: Institut zagalnoi ta neorganicnoi himii imeni V I Vernadskogo Nacional'na akademia nauk Ukraini

https://orcid.org/0000-0003-3173-0690

Ivan Shcherbatiuk

V I Vernadsky Institute of General and Inorganic Chemistry National Academy of Sciences of Ukraine: Institut zagalnoi ta neorganicnoi himii imeni V I Vernadskogo Nacional'na akademia nauk Ukraini

Vitaly Sirosh

V I Vernadsky Institute of General and Inorganic Chemistry National Academy of Sciences of Ukraine: Institut zagalnoi ta neorganicnoi himii imeni V I Vernadskogo Nacional'na akademia nauk Ukraini

Olexandr Potapenko

V I Vernadsky Institute of General and Inorganic Chemistry National Academy of Sciences of Ukraine: Institut zagalnoi ta neorganicnoi himii imeni V I Vernadskogo Nacional'na akademia nauk Ukraini

Serhii Solopan

V I Vernadsky Institute of General and Inorganic Chemistry National Academy of Sciences of Ukraine: Institut zagalnoi ta neorganicnoi himii imeni V I Vernadskogo Nacional'na akademia nauk Ukraini

Research Article

Keywords: Anatase-rutile anode, Surface morphology, Capacity, Li+ Diffusion, Current load

Posted Date: November 10th, 2025

DOI: https://doi.org/10.21203/rs.3.rs-7856805/v1

License: This work is licensed under a Creative Commons Attribution 4.0 International License.
Read Full License

The reasons capacity loss in Li-ion battery with anatase - rutile anode under the cycling

Katherine Pershina[1], Ivan Shcherbatiuk[1], Vitaly Sirosh[1], Olexandr Potapenko[1], Serhii Solopan[1]

Received: ……/Accepted …

Abstract X-ray powder diffraction analysis, scanning electron microscopy (SEM), energy dispersive spectroscopy (EDS), transmission electron microscopy (TEM), the Brunauer-Emmet-Teller method, and galvanostatic cycling were used to investigate phase content and morphology impact on capacity loss in a Li-ion battery with an anatase-rutile anode. Pore radii distributions were obtained from isotherms in terms of the density functional theory. The XRD patterns and TEM images detected the presence of two mixed TiO2 phases (anatase and rutile) with cube-like particle morphology and a quasi core-shell structure. The presence of two polymorphs of TiO_2 increases the crystallite size of anatase and rutile relative to single phases of anatase and rutile, the average pore size, and decreases the surface area of rutile. Experimental results demonstrate a correlation between crystallite

size and oxygen vacancies and capacity loss in a Li-ion battery with an anatase-rutile anode under galvanostatic cycling.

Keywords Anatase-rutile anode● **S**urface morphology● Capacity● Li^+ Diffusion● Current load

✉ Katherine Pershina
katherinepersh@gmail.com

[1] V.I. Vernadsky Institute of General and Inorganic Chemistry of the NAS of Ukraine, National Academy of Sciences of Ukraine, Kyiv, Ukraine

Introduction

TiO_2-based materials are possible candidates for replacing graphite in negative electrodes for Li-ion batteries due to their safety, low cost, and ability to deliver high specific power. The wide use of such materials is restrained because of the differences in the solid electrolyte interphase (SEI) formation on the surface of various titanium polymorphs [1, 2]. Although Li-ion intercalation/deintercalation in TiO_2 occurs within the stability window of the electrolyte, there are some reports about the formation of SEI observed on the surface of TiO_2 above 1.5 V vs. Li/Li^+. However, it is still questionable whether an SEI may be formed on the surface of TiO_2 phases similarly to the one formed on the surface of other materials for negative electrodes or whether its formation has different steps and features connected with phase content and size distribution of particles. Also, in recent years, the incorporation of oxygen vacancies into such anode materials has been demonstrated to improve electrical conductivity, cycling stability, and rate performance through experimental studies [3]. From electrochemical and morphological analysis, it appears that, upon cycling to more cathodic cut-off potentials, the anatase TiO_2 nanoparticles are becoming less active with the fast fading of the specific charge and an increase in the overpotential for the intercalation/deintercalation process [4, 5]. Under all conditions, oxygen vacancy formation is slightly more favorable in anatase than in rutile, while

titanium interstitials form more easily in rutile than anatase [6]. Research shows that under O-rich conditions, oxygen vacancies are the favored defect type, but both defect types have high formation energies. This suggests that while oxygen vacancies are more likely to form than titanium interstitials under oxygen-rich conditions, their formation still requires significant energy [7]. Some research suggests that controlling oxygen vacancy concentration and distribution could be key to optimizing Li-ion- and Na-ion transport in TiO_2-based electrode materials, with the specific effects depending on the crystal structure (anatase vs. rutile) being used [8]. In contrast to the more widely studied TiO_2 rutile, oxygen vacancies are not stable at the anatase (101) surface [9]. Therefore, the reason for capacity loss in a Li-ion battery with an anatase-rutile anode under cycling has not been fully identified. Therefore, in this work, the main objective was to identify the reasons for capacity loss in a Li-ion battery with an anatase-rutile anode under galvanostatic cycling connected with the inner structure and morphology of anatase/rutile mixed-phases of TiO_2 nanoparticles.

Results and Discussion

The X-ray powder diffraction analysis detected the main TiO_2 polymorph phases (anatase and rutile) in all samples prepared via alkaline hydrolysis of ortho-titanic acid: 53.8% rutile and 46.2% anatase (Fig. 1).

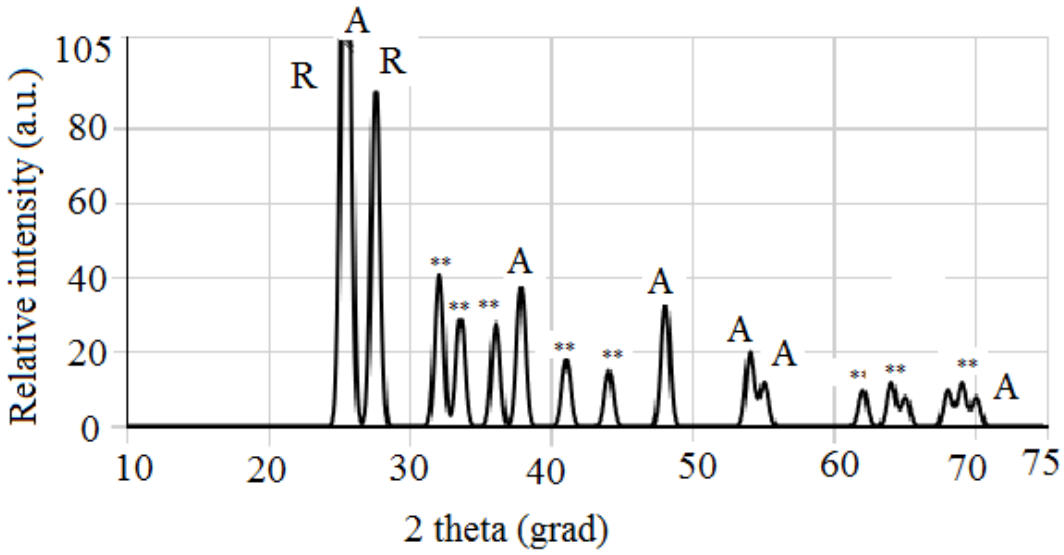


Fig. 1. X-ray powder patterns of the main TiO_2 polymorphs phases in samples prepared via alkaline hydrolysis of the ortho-titanic acid. * A denotes anatase and R denotes rutile; - A+R denotes close contact between anatase and rutile (mixed phases)**.**

Both phases (anatase and rutile) (Table 1) have a tetragonal crystal system with space group I 41/ a m d (141) for anatase, and P 42/m n m for rutile. The unit cell parameter for anatase is 3.7842 Å, and for rutile - 4.5922 Å (Table 2).

The morphology of the TiO_2 nanoparticles was characterized by TEM and SEM (Fig. 2, 3). The sample is a mixture of anatase and rutile phases, which exhibit cube-like particle morphology with particles sizes {of approximately 75–225 nm in length, and 80–130 nm in width). As well as

cuboid particle morphology (with sizes of approximately 20–50 nm in length, and 20–40 nm in width), and some irregularly shaped particles with a quasi core-shell structure were detected.

Table 1 TiO_2 polymorphs in the samples fixed on XDR spectra

TiO_2 polymorphs	d [Å]	Entry N°.
Anatase	3.5142; 2.4305; 2.3781; 2.3324;1.8921; 1.7471; 1.6997; 1.6663; 1.4933; 1.4807; 1.3389	96-901-5930; 96-900-9087; 96-720-6076; 96-500-0224; 96-900-8215; 96-900-8216; 96-900-8217
Rutile	3.2466; 2.4869; 2.2960; 2.1869; 2.0542; 1.6877; 1.6663; 1.6242; 1.4807; 1.4529; 1.3611; 1.3468	96-900-9084; 96-900-7433; 96-900-1682;96-900-7532; 96-900-4142; 96-901-5663; 96-410-2356; 96-900-4143; 96-900-4144; 96-900-4145

Table 2 The main Crystal systems of TiO_2 polymorphs detected in samples

TiO_2 polymorphs	Crystal system	Space group	Unit cell, A	Calc. Density, g/cm^3
Anatase	tetragonal	I 41/ a m d (141)	a- 3,78420 b- 9,51460	3,894
Rutile	tetragonal	P 42/ m n m	a- 4,5922 b- 2,9574	4,233

The surface of such mixed phases has a morphology like a conglomerate with various pore radii and an average particle size of up to micrometers (Fig. 3).

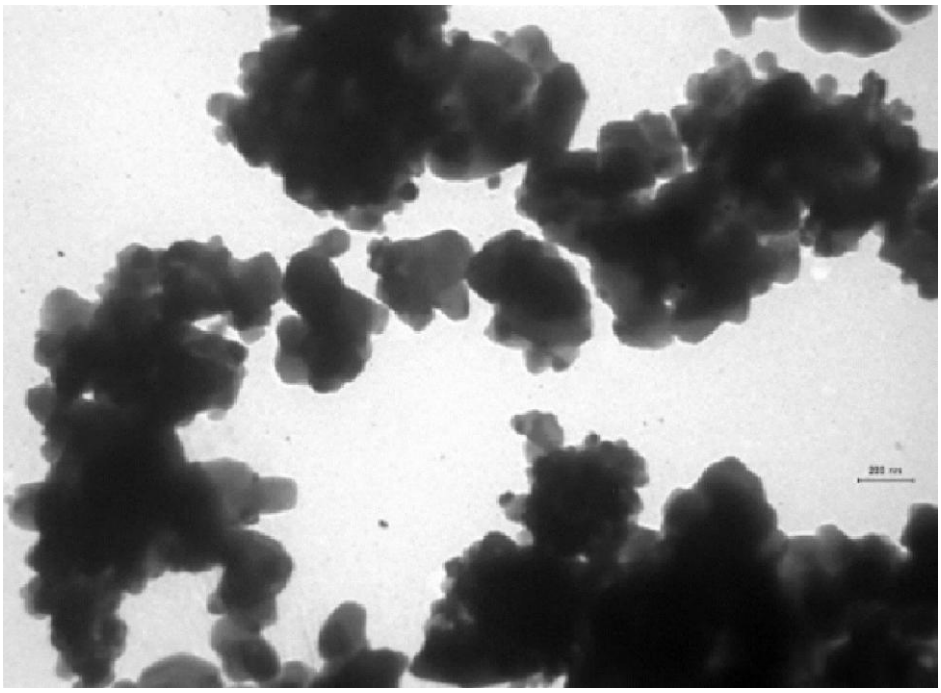


Fig.2. TEM images of the anatase/rutile samples

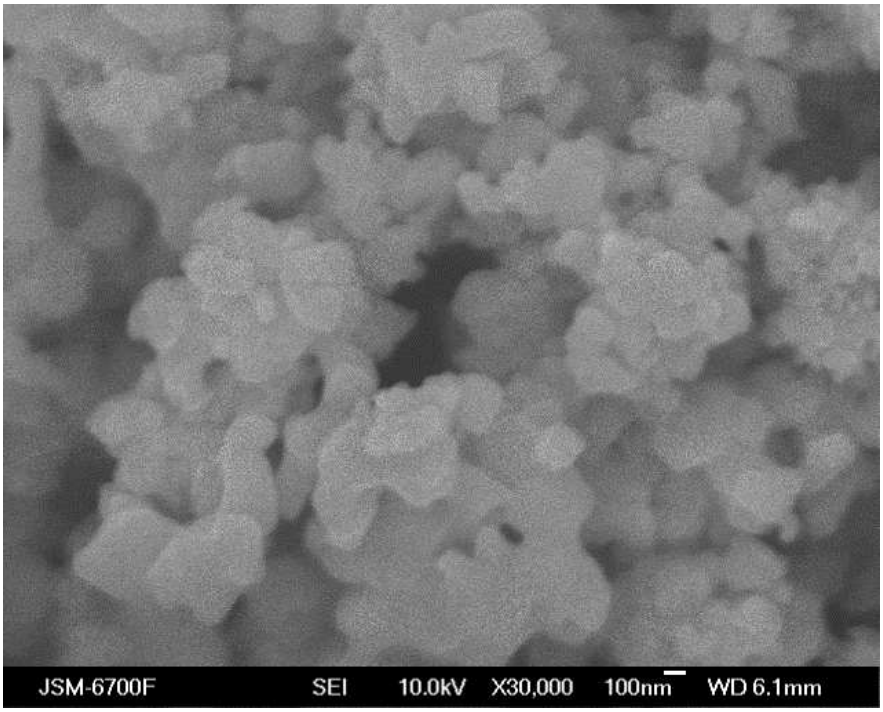


Fig.3. SEM images of the anatase/rutile samples

Table 3 . Morphological data of anatase/rutile samples

Crystallite size* (nm)	Average pore size, nm	Surface area ($m^2 \cdot g^{-1}$)	Cumulative pore volume ($cm^3 g^{-1}$)	Porosity, %
91,46 (R). 376,05 (A)	1,75; 30	8,51	$1,1 \div 2.09 \cdot 10^{-2}$	2.6 ± 0.2

*Calculated from XRD data using Eq. (1). A denotes anatase and R denotes rutile

The presence of two polymorphs of TiO_2 increases the crystallite size of anatase and rutile relative to single phases of pure anatase and rutile, increases the average pore size, and decreases the surface area of rutile (Table 3).

The close anatase-rutile contact creates opportunities to change the quantity of surface oxygen vacancies [3, 8] and additional surface defects [8] connected to Li-ion intercalation via the rutile surface. According to EDS analysis (Table 4), the quantity of oxygen on the surface is several times higher than the stoichiometric amount in TiO_2. This may be the reason for decreasing capacity due to the increased surface oxygen content competing with Li ions (Table 4).

Table 4. Surface oxygen amount and capacity value of anatase/rutile samples

Stehiometric amount of O in TiO_2, %	Surface amount O in anatase/rutile sample, % (EDS data)	C, F / g (10^{-2}÷10^{1} Hz)	C, F/g (10^{3}÷10^{5} Hz)
40	80±0,5	3.17±0.9	0.68±0.03

This agrees with the opinion that the main point vacancy on the rutile TiO_2 (110) surface is the positively charged bridging-oxygen vacancy (BOV^+) [9, 10]. Oxygen defects are significantly more stable at subsurface than at surface sites in the case of anatase surfaces, whereas bridging oxygen sites are favored for O vacancies at rutile TiO_2 (110) [11]. In the case of doping with a foreign element (for example, Li or Na), this usually results in plenty of non-intrinsic defects in the TiO_2 crystal lattice. Self-doping with intrinsic defects such as Ti^{3+} and oxygen vacancies has a similar effect to non-intrinsic defects, but does not introduce foreign defects. Therefore, the presence of oxygen vacancies should compete with metals in non-intrinsic defect formation and regulate Li+ diffusion:

$$nTiO_2 + V_o^+ + xLi^+ + xe \rightarrow Li_xTi_nO_{2n-1} \ (4.1 \leq 2n-1 \leq 4.7) \quad (1)$$

As TiO_2 is an intercalation anode, it follows a basic mechanism of Li^+ insertion and extraction during the charge/discharge cycles:

$$TiO_2 + xLi^+ + xe \rightarrow Li_xTiO_2 \ \ (1 \leq x \leq 0) \quad (2)$$

The presence of rutile oxygen vacancies should be a main factor in anode capacity lost because of dominate role of surface O-vacancies formation relatively anatase. Such point of view could be explain the behavior of the anatase-rutile anode during charge/discharge cycling (Fig.4, 5).

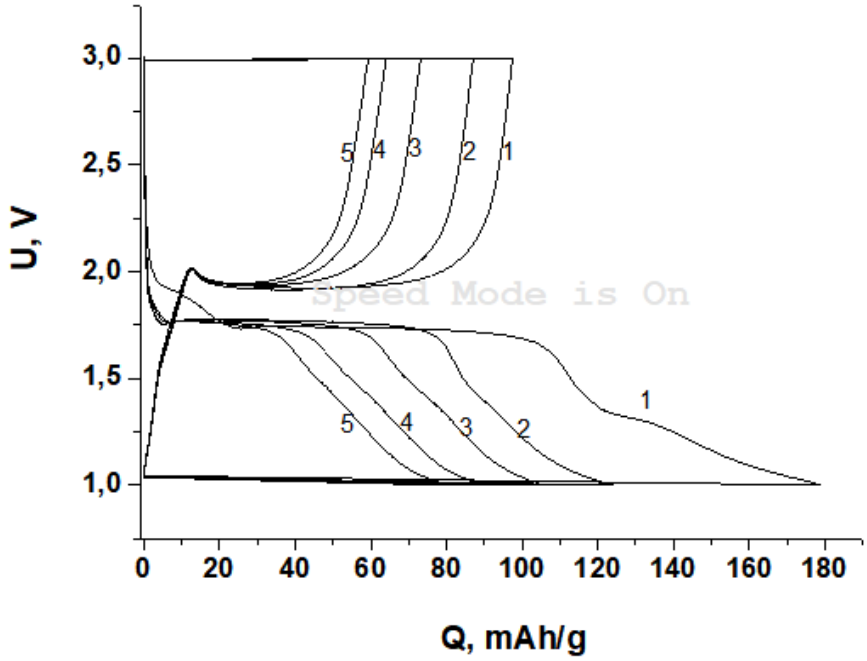


Fig.4. Charge-discharge voltage profile of the Li/TiO_2 (anatase-rutile) system

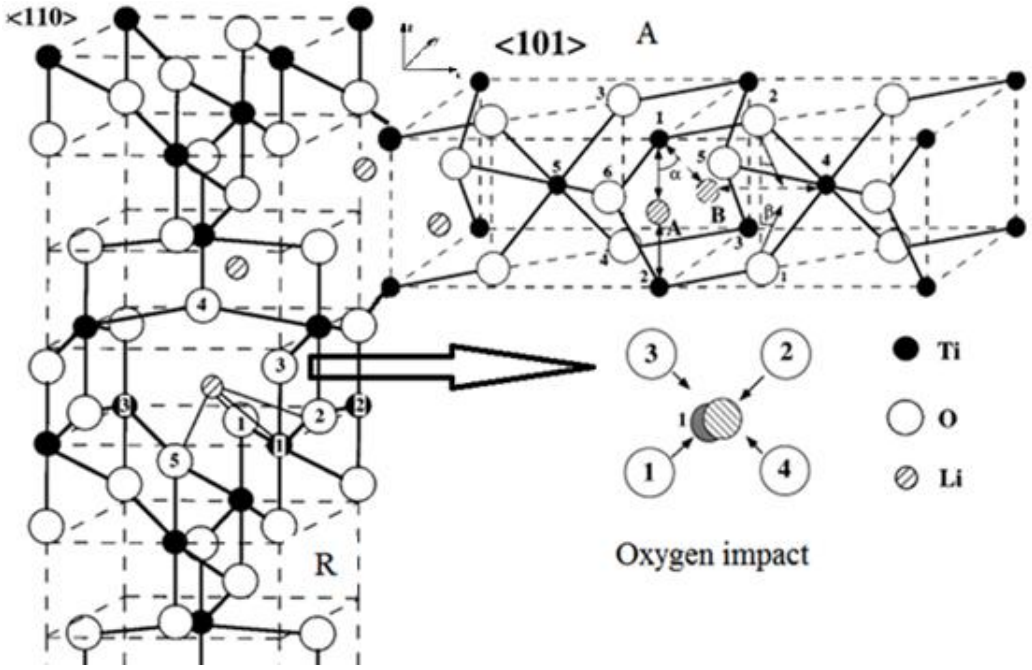


Fig. 5. Scheme of competitive movement of Li-ions and O-vacancies. A- anatase, R- rutile

Electrochemical measurements of lithium and mixed anatase–rutile electrodes reveal that increasing the potential sweep rate results in higher peak currents and a positive shift of the peak potential during deintercalation. Conversely, during lithium intercalation into the TiO_2 lattice, the peak current shifts toward lower potentials (Fig. 6). The magnitude of the voltage shift is attributed to the limited electronic conductivity of the electrode, determined by the intrinsic resistivity of TiO_2 and influenced by crystal structure, defect density, and temperature. Additionally, a minor feature ("wave") observed in the potential range ΔE = 1.6–1.9 V (vs. Li^+/Li) is presumably associated with the presence of the rutile phase [8–11].

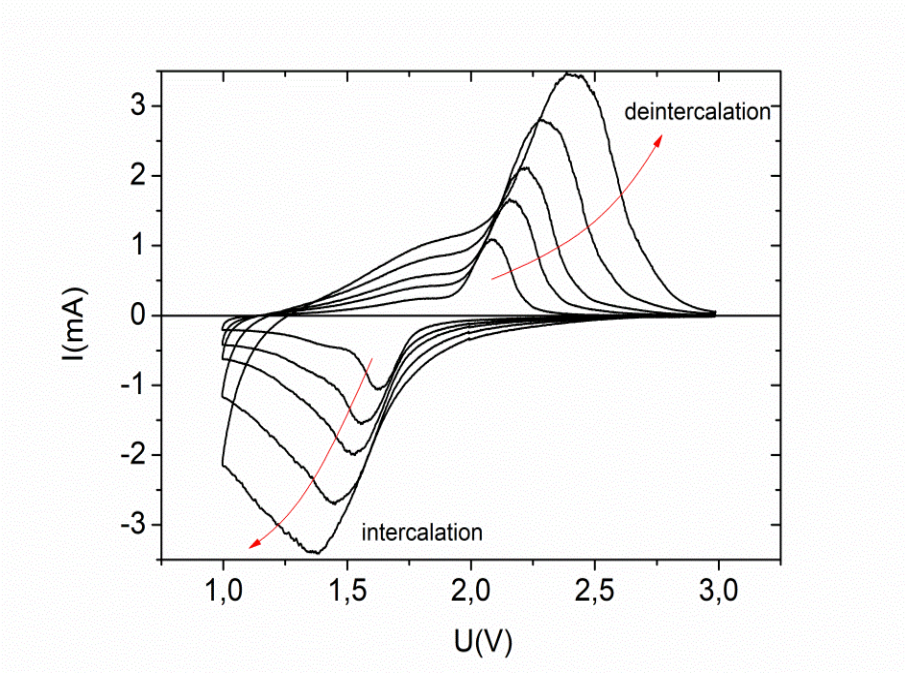


Fig.6. CVA of rutile/anatase TiO_2 sample at different potential scan rates: 0.1; 0.2; 0.3; 0.5 and 0.8 mV/sec. t = 25 ^{O}C.

Based on CVA curves the diffusion coefficients in the intercalation and deintercalation Li^+ ions at the low current density (i = 0.05C) were calculated:

$$C_{Li} = \frac{Q*m}{F*V} \quad (3)$$

Q – specific capacity (C/g or mAhm/g); m – mass of active substance (g); F – Faraday constant (96485 C/mol); V – electrode volume (cm^3).

$$D_{Li} = \left(\frac{i_p}{k*\vartheta^{1/2}}\right)^2 \quad (4)$$

The linear i_p – f(√υ) relationship is an indication of diffusion control of the lithium ion intercalation reaction (fig.7).

The slope of this line is:

$$i_p = k*\vartheta^{\frac{1}{2}} + b \quad \text{or} \quad k = 0.131\ \frac{A}{(\frac{V}{sec})^{1/2}} \quad (5)$$

Hence, the diffusion coefficient of lithium ions into/from the TiO_2 structure is:

$$D_{Li} = (\frac{0.131}{2.69*10^5*2*0.0064})^2 = 1.45*10^{-9}\ cm^2s^{-1}$$ - deintercalation

$$D_{Li} = 1.42*10^{-9}\ cm^2s^{-1}$$ - intercalation

According to impedance spectroscopy data under various current load impact lithium diffusion coefficient strongly depends on current density and quantity of charge/discharge cycles (Table 5, fig. 8, 9).

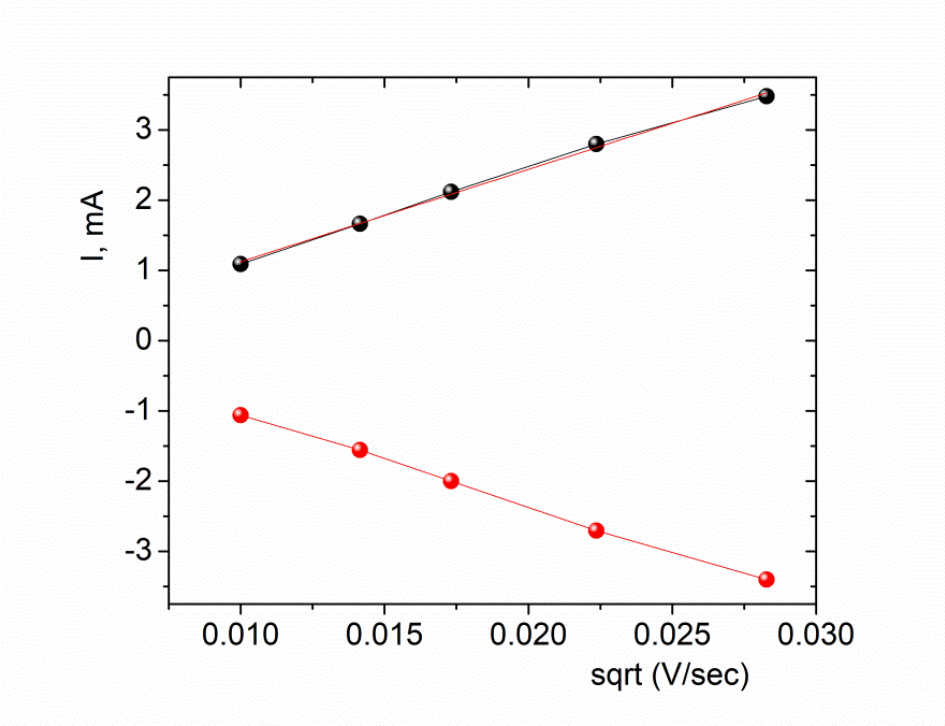
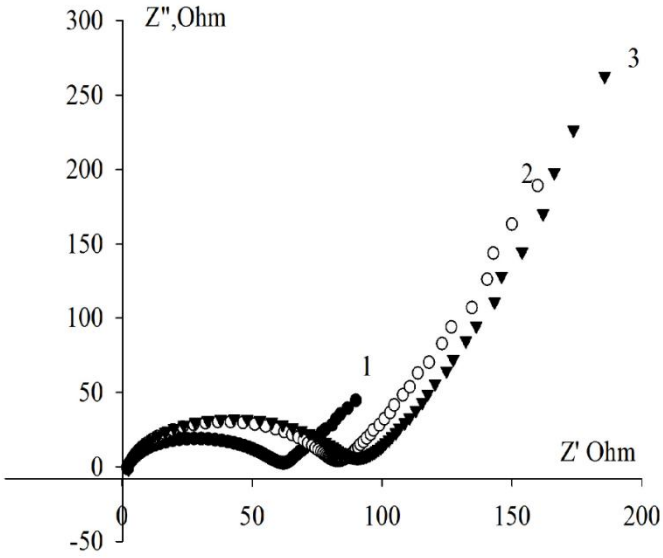


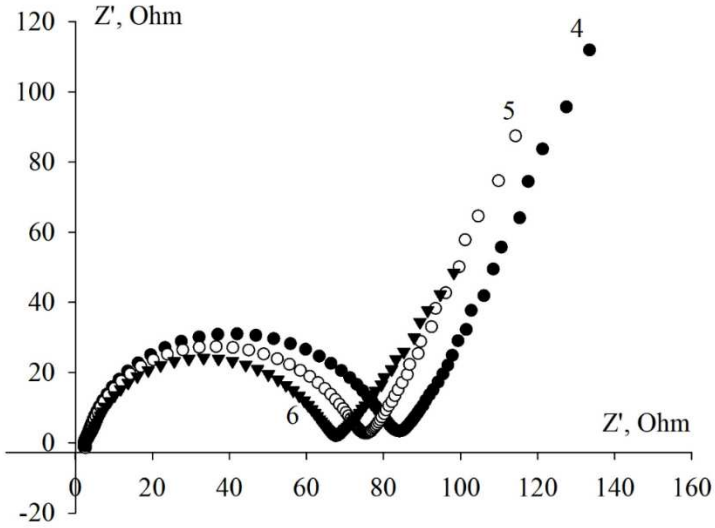
Fig.7. Current density changes as a function of the square root of the potential sweep rate $i_p - f(\sqrt{\upsilon})$

Table 5. Apparent diffusion coefficients of Li^+ in Anatase/Rutile anode calculated from EIS

Current density, mAhm/g 1C = 335 mAhm/g	C/2	C/5	C/10	C/20
D^{app}_{Li+} x $10^{-9}cm^2s^{-1}$	2,44	1,65	1,35	0,93



1



2

3

4 **Fig. 8.** Impedance spectra of the rutile/anatase TiO_2 samples under
5 various current density: 1- C/20 (5 charge/discharge cycles); 2- C/20 (15
6 charge/discharge cycles); 3- C/10 (25 charge/discharge cycles); 4 - C/5 (60
7 charge/discharge cycles); 5 - C/2 (60 charge/discharge cycles); 6- 5 - C/2
8 (110 charge/discharge cycle

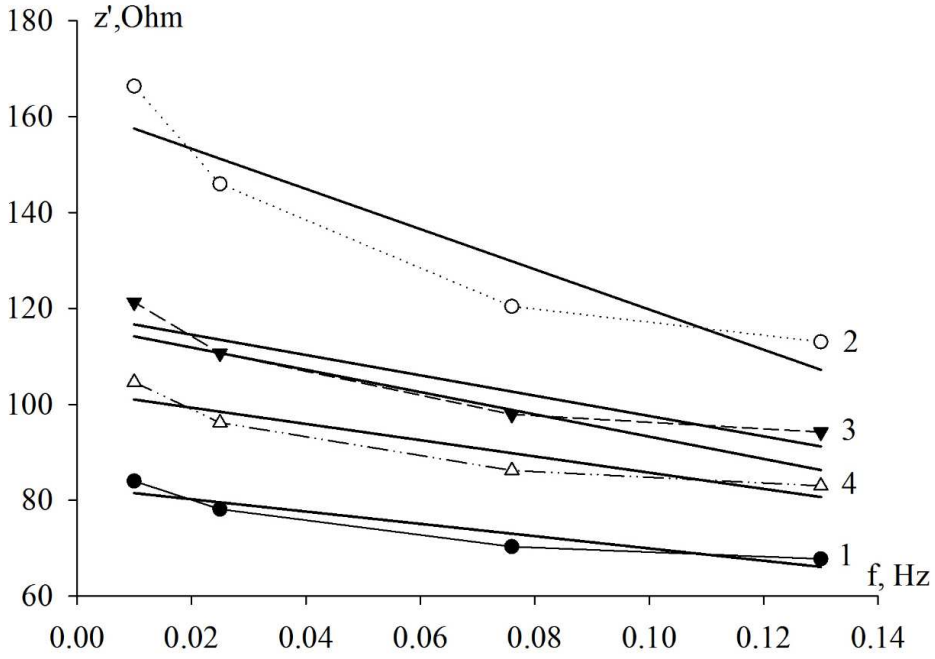


Fig. 9. Average Warburg coefficients dependence in the rutile/anatase TiO_2 samples under various current density: 1 - C/2; 2 - C/20; 3- C/10; 4 - C/5.

For isolated lithium in rutile, the diffusion coefficient at room temperature is approximately 9×10^{-5} cm²/s (or 9.1×10^{-6} cm²/s from DFT calculations), with an activation energy of 0.05-0.06 eV [12]. However, the diffusion coefficient is strongly concentration-dependent and decreases significantly with increasing Li content - at 50% Li concentration, the diffusivity is three orders of magnitude slower than at 10% Li concentration [13]. The diffusion in rutile is highly anisotropic, with the diffusion coefficient parallel to the c-axis being at least 10^8 times larger than perpendicular to it [14]. So Li - ions diffuse one-dimensionally through

channels along the c-axis. For anatase thin films, the Li-ion diffusion coefficient near the insertion peak is approximately 2.6×10^{-14} cm²/s and near the extraction peak is 8.8×10^{-14} cm²/s [15]. For nanoporous anatase films at 25°C, the diffusion coefficient is approximately 2×10^{-17} cm²/s for insertion and 4×10^{-17} cm²/s for extraction, with activation energies of 0.4 eV for insertion and 0.5 eV for extraction [16]. But, as cathode material, rutile TiO_2 exhibits slower lithium diffusion than anatase TiO_2 though the specific values depend significantly on morphology, crystallinity, particle size, and Li concentration. The experimental values vary widely across studies depending on these factors [17]. Hence, the diffusion of Li ions in mixed anatase/rutile electrode have a middle diffusion coefficient between isolated lithium in rutile and nanoporous anatase. The presence of rutile increase the Li diffusion coefficient more than five orders comparatively pure anatase.

Discharge-charge curves of TiO_2 in a lithium half-cell at a current density of ~ 17 $mA \cdot g^{-1}$ (C/20) demonstrate the characteristic features close to nanocrystalline anatase TiO_2 after intercalation and subsequent deintercalation (fig. 10). In the potential region between the initial OCP and ~1.8 V, a voltage profile may be indicate the formation of a solid solution, which corresponds to the initial introduction of lithium into the anatase TiO_2 structure to approximately $Li_{0.09}TiO_2$ with preserved anatase phase. The

main plateau at approximately 1.8 V corresponds to the first phase transition from lithium-depleted anatase to lithium-enriched titanate, leading to the formation of a composition of approximately $Li_{0.5}TiO_2$. After this main voltage plateau, the potential drops again, and at approximately 1.5 V a second plateau is observed, corresponding to the second phase transition from enriched lithium titanate, corresponding to the second phase transition [18].

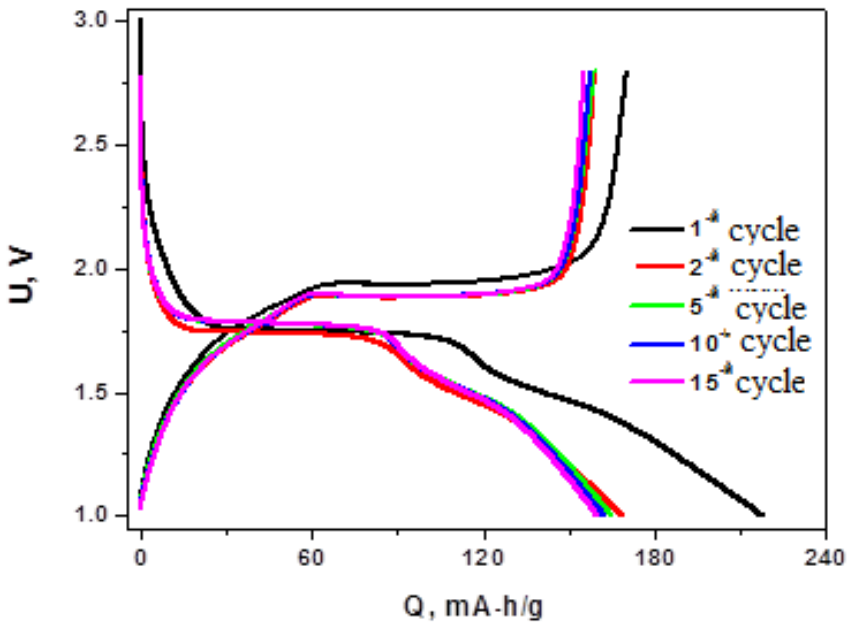


Fig.10. Charge-discharge curves of the Li-TiO_2 cell during cyclings under current density C/20.

A significant irreversible capacity loss (~22%) occurs after the first discharge. The Coulombic efficiency at C/20 is high after the first cycle

(fig.10). The first discharge capacity is 218 mAh g^{-1} (65% of the theoretical capacity of TiO2), and the high reverse discharge capacity of 169 mAh g^{-1} after the first cycle remains at 160 mAh g^{-1} after 15 cycles at this current density (Fig. 11). At C/2, the specific discharge capacity of TiO_2 is about 120 mAh g^{-1}. However, with increasing charge-discharge current density, the specific capacity decreases to 60 mAh g^{-1} (2C). However, when the current density decreases again to C/2, the initial specific capacity can be restore, which indicates the high structural stability of the synthesized TiO_2.

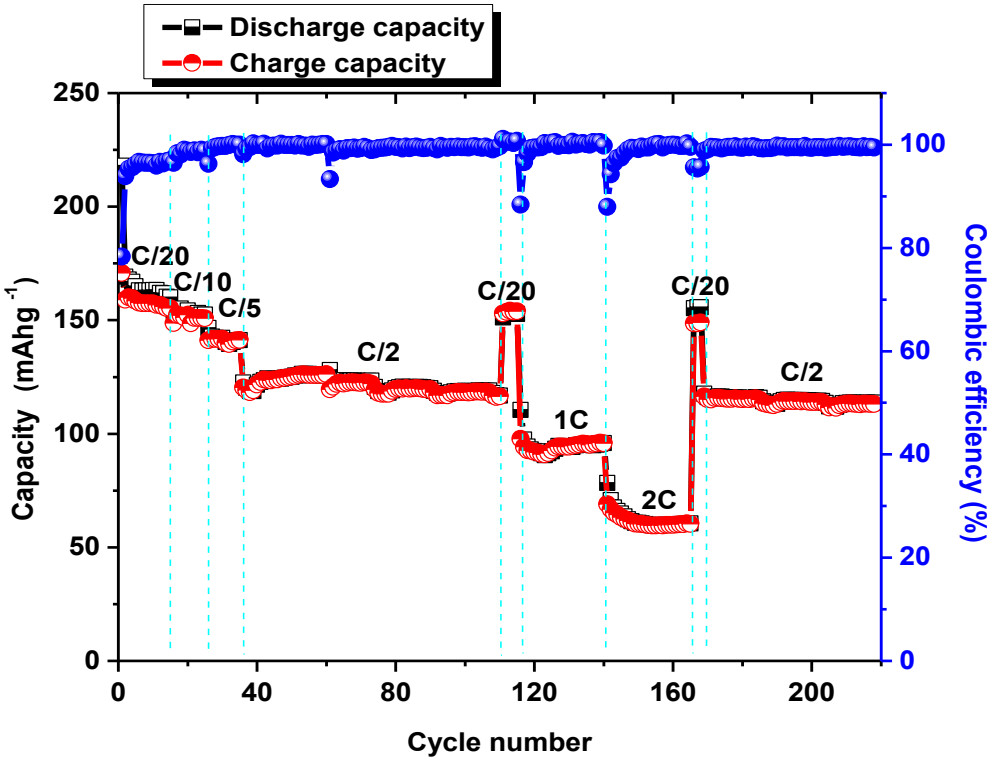


Fig.11. Changes in the capacity data of TiO_2 during cycling under various current density (from C/20 up to 2C).

According to the experimental dependences (fig.12), with increasing current load, polarization increases, which leads to a reduction of the main plateau, but, unlike the discharge curves, it is still present even for applied current densities up to 2C (although its position shifts towards higher voltages with increasing current load). This behavior indicates lower kinetic limitations for lithium deintercalation than for lithium intercalation due to the low electronic conductivity in the composite electrode structure [19.20].

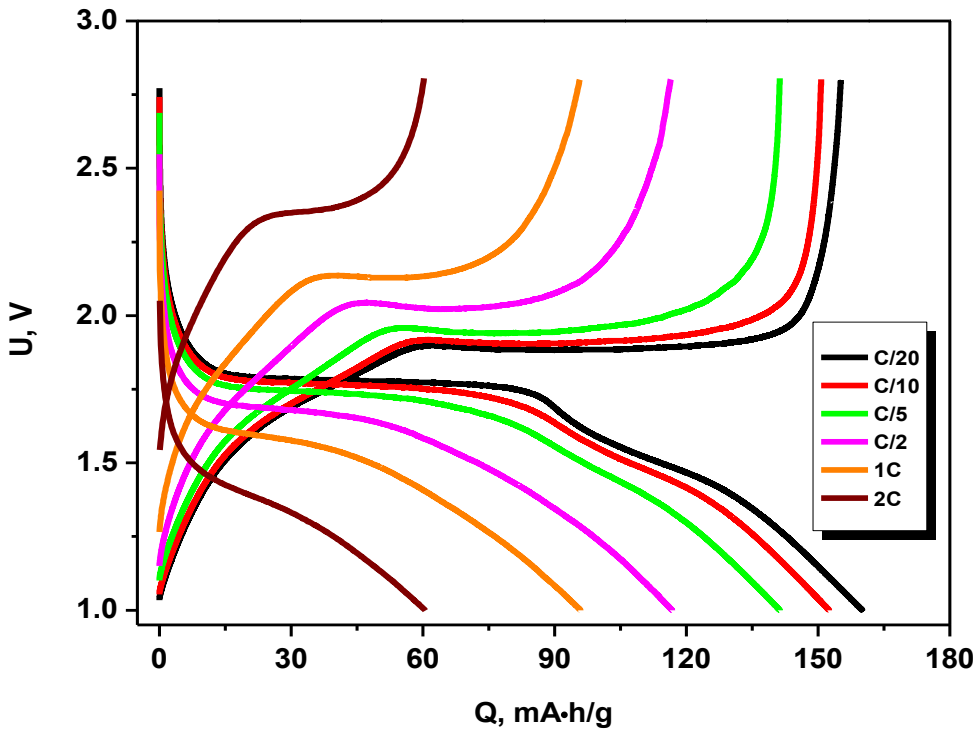


Fig.12. Charge-discharge curves of the Li-TiO_2 cell during cyclings under various current density (from C/20 up to 2C).

Conclusion

Based on experimental results a direct correlation is established between the anatase–rutile surface condition, oxygen vacancy concentration, galvanostatic cycling duration, pore distribution, crystallite size, and capacity loss. The X-ray powder diffraction analysis detected the main TiO_2 polymorphs phases (Anatase and Rutile) in all samples prepared via alkaline hydrolysis of the ortho-titanic acid with containing. The morphology of the TiO_2 nanoparticles was characterized by SEM, EDS, TEM and Emmet-Teller methods. This mixture of anatase and rutile phase, which has a cube-like particle morphology with a size about 75–225 nm in length and 80–130 nm in width. A cuboid particle morphology with a size about 20–50 nm in length and 20–40 nm in width, and some irregularly shaped particles with quasi core-shell structure. The surface of such mixed phases has morphology like a conglomerate with various pore radiuses and the average size of particles up to micrometers. The presence of two polymorphs of TiO_2 in contact increases the crystallite size of anatase and rutile relatively single phases of pure anatase and rutile, average pore size, and decreases the surface area of rutile. It have been shown that the presence of rutile oxygen vacancies may be a main factor in anode capacity lost because of dominate role of surface O-vacancies formation relatively anatase. CVA and EIS experiments were shown that the presence of rutile increase the Li diffusion coefficient

more than five orders comparatively pure anatase. This is the reason of decreasing kinetic limitations for lithium deintercalation than for lithium intercalation in the Li-TiO_2 cells with mixed anatase/rutile electrode.

Experimental

Anatase/rutile samples (with size 90-230 nm) were synthesized using alkaline hydrolysis of $TiCl_4$ solutions [21]. The samples were dried at 383 K for 24 h with further thermal treatment at 500-5120 K in the air for 45 hours.

The structural investigation and *X-ray* powder diffraction analysis were performed on a (Cu-Ka radiation) and a Bragg 2θ configuration.. The phase content and crystallite size estimations were performed automatically using Match 3.0 software. The average crystallite size in this software is calculated from selected peaks/lines using Scherrer's formula. The average crystallite size is calculated automatically by using all phases with crystallites and the sizes of crystallite. The Scherrer constant used in calculation of crystallite size was 0.94. SEM images and EDX data obtained on a JEOL F-6301 scanning electron microscope. A high resolution TEM images were obtained on a JEM 2010 microscope. Specific surface areas and pore size distributions for the synthesized samples were calculated from nitrogen adsorption/desorption curves (NOVA 2200e, Quantachrome, USA)

using the Nova Win 2.0 software. Before measurements, the samples were vacuum-treated overnight at 120 ^{0}C. The total surface area of the materials S_{total} was calculated by the Brunauer-Emmet-Teller method (BET). The total pore volume (V_{total}) was calculated from the volume of nitrogen adsorbed converted to liquid at a pressure close to $P/P_0 = 1$. To acquire the volume and radii of mesopores ($V_{meso,}$ R_{meso}), Barrett-Joyner-Halenda (BJH) were used. The average pore radii (R_{pore}) was determined from the total pore volume (V_{total}) of the materials and its specific surface area (S_{total}) by equation $R_{pore} = 2V_{total}/S_{total}$. The micropore volume ($V_{micro}$) was calculated by subtracting the value of $V_{meso}$from V_{total}. Pore radii distributions were obtained from isotherms in terms of the density functional theory (DFT). described how was the calculation performed. Pore distribution was calculated using NOVA software with mathematical apparatus based on DFT. In case of this theory pore volumes were defined by their diameter (∅). The volume of micropores (∅ ≤ 2 nm) was obtained from the DR method ($V_{micro}(N_2)$). The volume of mesopores (2 < ∅ ≤ 50 nm) was calculated by abstracting the amount of N_2 adsorbed at $p/p_o = 0.3$ from that adsorbed at $p/p_o = 0.8$ ($V_{meso}(N_2)$), and the total volume ($V_{Total}(N_2)$) was considered as the amount of N_2 adsorbed at p/po = 0.95. Liquid densities of the adsorbates were obtained from the literature (0.808 g cm^{-3} for N_2). Porosity distributions were determined according to density-functional theory (DFT) using NOVA

software and applying the “2D-NLDFT heterogeneous Surface” model for N_2 adsorption. Mean pore sizes were further determined by applying the Barrett–Joyner–Halenda (BJH) method to the desorption curves, using a Kruk–Jaroniec–Sayari correction and thickness curve [21].

EIS measurements were performed on an electrochemical module Autolab 30 PGSTAT301N Metrohm Autolab in a two-electrode cell (disk cell) in the frequency range $10^{-1} \div 10^{5}$ Hz. The calculation results were received using ZView2 software. Electrochemical studies of the mock-ups were carried out using a high-voltage galvanostat MTech-G410 (MTech Lab, Ukraine) in a potential range of 1.0 ÷ 2.8 V and a density range of C/20 to 2C. The value of the cycle flow was determined at 1 C = 335 mA/g. All testing performed out at a temperature of 25±1°C.

Classical Randles–Sevchik equation for a semi-infinite diffusion of Li+ into anode can be applied for calculation diffusion coefficient by CVA data:

$$i_p = (2.69 * 10^5) * n^{\frac{3}{2}} * A * D_{Li}^{\frac{1}{2}} * C_{Li} * \vartheta^{1/2} \quad (6)$$

i_p – peak current in (A); n – number of electrons in the reaction (n = 1); A – electrode area (cm^2); D_{Li} – lithium diffusion coefficient (cm^2/sec); C_{Li} – lithium ion concentration in the electrode volume (mol/cm^3); υ – potential scan rate (V/sec).

These coefficients calculated with taking into account the next conditions of experiment relevancy (presence of a reversible electrochemical reaction; presence of diffusion control; absence of chemical transformations after the electron transfer; absence of significant temperature fluctuations during the charge transfer process).

Calculation of Warburg coefficients and lithium diffusion coefficients were performed from EIS data from linear part Nyquist plot (straight line with slope ≈ 1 (45° angle)) in a frequencies < 1 Hz. For calculation took Z' (real impedance) and corresponding frequencies (ω) for each point from this linear region:

$$\sigma = Z'\omega^{-1/2} \quad (7)$$

$$D = (RT)^2/(2n^2F^2A^2C^2\sigma^2) \quad (8)$$

D -diffusion coefficient (cm^2/s); R - gas constant; T - temperature (K); n - number of electrons (typically 1 for Li^+); F - Faraday constant; A - electrode area (cm^2); C - Li^+ concentration (mol/cm^3); σ - Warburg coefficient ($\Omega \cdot s^{(-1/2)}$).

Electrodes production: the synthesized TiO_2 powder was ground in an agate mortar and sieved through a sieve (cell size ø≤80 μm). A mixture of components was prepared from the active material (TiO_2), an electrically conductive additive (acetylene black) and a polymer compound (PVDF,

Solef 6020) in the N-methyl-2-pyrolidonium (NMP, Sigma-Aldrich) media. The mass ratio of components in the samples became 80:10:10. Homogenization of the mixture was carried out using a high-speed stirrer at 750 rpm for 1 hour. The resulting paste applied to aluminum foil using a Doctor Blade applicator (~200 μm) and dried in a drying oven at a temperature of 65°C for 4 hour. Electrodes were cut out with a working surface of the 2 cm^2 from the dried electrode strip, followed by thickening of the electrode mass in a press. Then the electrodes before preparing the mock-ups, were dried at a temperature of 120°C for 2 hours in a vacuum. The mass of the active material of the electrodes varied between 3.2 – 3.3 mg/cm^2. The disk mock-ups in size 20x16 with a lithium electrode have been used to determine the power characteristics of TiO_2 anodes. An electrolyte was solution of the LiPF6 (1 mol/l) in the mixture of solvents EC:DMC:DEC (v/v/v = 1:1:1). Polypropylene film (Celgard 2500) was used as a separator. An assembly of the element models was carried out in a glove box with an inert atmosphere.

Acknowledgements The authors would like to express their deep appreciation to the National Academy of Sciences of Ukraine (NASU) for the financial support our work (SR $N^0$0122U200365).

Declarations Authors haven't any conflicts of interests and competing interests

References

1. Madej E, Ventosa E, Klink S, Schuhmann W, La Mantia F (2014) *Phys Chem Chem Phys* 16:7939. DOI: 10.1039/C4CP00630E

2. Paul S, Rahman MA, Islam MS, Islam MR, Siddiqui SET (2022) *Battery Energy* 1:20220018. DOI: 10.1002/bte2.20220018

3. Yeh HL, Tai SH, Hsieh CM, Chang BK (2018) *J Phys Chem C* 122:19447. DOI: 10.1021/acs.jpcc.8b06540

4. Globa NI, Shmatok YV, Lisnycha TV, Kirillov SA (2021) *ECS Trans* 105:61. DOI 10.1149/10501.0061ecst.

5. Globa N, Lisnycha T, Shmatok Y, Sirosh V, Kirillov S (2020) *Ukr Chem J* 86:14 DOI: 10.33609/2708-129X.86.9.2020.14-27.

6. Dawson JA, Robertson J (2016) *J Phys Chem C* 120:22910. DOI: 10.1021/acs.jpcc.6b08842.

7. Usui H, Domi Y, Sakaguchi H (2023) *ACS Appl Energy Mater* 6:4089. DOI: 10.1021/acsaem.3c00266.

8. Medvids A, Varnagiris S, Letko E, Milcius D, Grase L, Gaidukovs S, Mimura H (2020) *Mater Sci Semicond Process* 106:104776. DOI:10.1016/j.mssp.2019.104776.

9. Elahifard M, Sadrian MR, Mirzanejad A, Behjatmanesh-Ardakani R, Ahmadvand S (2020) *Catalysts* 10:397. DOI: 10.3390/catal10040397.

10. Wang SG, Wen XD, Cao DB, Li YW, Wang J, Jiao H (2005) *Surf Sci* 577:69. DOI:10.1016/j.susc.2004.12.017.

11. Hou L, Zhang M, Guan Z, Li Q, Yang J (2018) *Appl Surf Sci* 428:640

12. Kerisit S, Rosso KM, Yang Z, Liu J (2009) *J Phys Chem C* 113:20998. DOI:10.1016/j.apsusc.2017.09.144.

13. Yildirim H, Greeley JP, Sankaranarayanan SK (2012) *Phys Chem Chem Phys* 14:4565. DOI: 10.1039/C2CP22731B.

14. Pfanzelt M, Kubiak P, Fleischhammer M, Wohlfahrt-Mehrens M (2011) *J Power Sources* 196:6815. DOI:10.1016/j.jpowsour.2010.09.109.

15. Moitzheim S, De Gendt S, Vereecken PM (2019) *J Electrochem Soc* 166:A1. DOI: 10.1149/2.1091816jes.

16. Lindström H, Södergren S, Solbrand A, Rensmo H, Hjelm J, Hagfeldt A, Lindquist SE (1997) *J Phys Chem B* 101:7717. DOI:10.1021/jp970490q.

17. Kanamura K, Yuasa K, Takehara Z (1987) *J Power Sources* 20:127. DOI: 10.1016/0378-7753(87)80101-5.

18. Lafont U, Carta D, Mountjoy G, Chadwick AV, Kelder EM (2010) *J Phys Chem C* 114:1372. DOI: 10.1021/jp908786t.

19. Bresser D, Paillard E, Binetti E, Krueger S, Striccoli M, Winter M, Passerini S (2012) *J Power Sources* 206:301. DOI:10.1016/j.jpowsour.2011.12.051.

20. Moretti A, Kim GT, Bresser D, Renger K, Paillard E, Marassi R, Winter M, Passerini S (2013) *J Power Sources* 221:419. DOI:10.1016/j.jpowsour.2012.07.142.

21. Shcherbatiuk IM, Lisnycha TV, Pershina KD (2025) *Chem Phys Technol Surf* 16:1. DOI:10.15407/hftp16.01.039.